Check for updates

Interfacial engineering of tungstic disulfide–carbide heterojunction for high-current-density hydrogen evolution†

TaiKun Wang,[ab] Zhaoan Hong,[ab] Fapeng Sun,[b] Bicheng Wang,[ab] Chuanyong Jian*[b] and Wei Liu [iD] *[b]

Developing low-cost and high-efficiency electrocatalysts to electrolyze water is an effective method for large-scale hydrogen production. For large-scale commercial applications, it is crucial to call for more efficient electrocatalysts with high-current density (≥ 1000 mA cm^{-2}). However, it is challenging to simultaneously promote the large-scale production and hydrogen evolution reaction (HER) activity of these hydrogen catalysts. Herein, we report the large area tungstic disulfide–carbide (W/WS$_2$–WC) heterojunction electrode vertically grown on an industrial-grade tungsten substrate by the solid-state synthesis method. The W/WS$_2$–WC heterojunction electrode achieves a low overpotential of 473 mV at 1000 mA cm^{-2} in alkaline electrolytes.

1. Introduction

As a renewable and sustainable energy carrier, hydrogen (H$_2$) has been considered a promising alternative to natural fossil fuels due to its high mass-energy density, cleanliness, and carbon neutrality.[1–3] Water electrolysis is one of the most feasible and economical methods for scalable hydrogen production by electricity from a sustainable energy source such as solar and wind.[4–6] Although platinum-group-metals (PGM) are generally considered the most efficient electrocatalysts toward hydrogen evolution reaction (HER) in acid media, alkaline water electrolysis is the most widely-used technology for hydrogen production in the industry due to the robustness of the electrode materials, long operating life, and cheap electrolyzer construction. HER kinetics in alkaline solutions involves two critical steps: H$_2$O dissociation (H$_2$O + M + e$^-$ → M–H$_{ad}$ + OH$^-$, where M stands for the active site and is H$_{ad}$ adsorbates); and H$_{ad}$ recombination (M–H$_{ad}$ + H$_2$O + e$^-$ → M + H$_2$ + OH$^-$ or 2H$_{ad}$ → H$_2$).[7–10] Interestingly, compared with acid electrolysis, the H$_2$O dissociation step can be added in alkaline HER, and the adsorption free energy of H to the catalyst surface ($\Delta G_{H_{ad}}$) remains an effective descriptor.[11,12] Unfortunately, the HER kinetics of the Pt-based catalysts in alkaline solutions generally is roughly two to three orders of magnitude lower than

that in acidic solutions due to the sluggish H$_2$O dissociation step, hindering its practical use for hydrogen production.[13,14] Many transition-metal-based compounds feature high capability for cleaving the H–OH bond, and they can serve as the co-catalysts to couple with Pt or other HER electrocatalysts for boosting the alkaline HER kinetics.[15] It should be noted that the modulation of the interface structure is a potential approach. Previous works have demonstrated that interface engineering can significantly modulate the interfacial electronic structure in heterojunctions, highly preserve exposed active sites, and thus enhance the catalytic performance.[16,17]

Among various TMCs, tungsten carbide (WC) presents Pt-like behavior in HER, which is attributed to the relative electronic density of states to Pt around the Fermi level.[18,19] For example, Wang *et al.* have presented a tungsten oxide/carbide surface heterojunction catalyst (SHC), which can serve as an excellent activity for the HER. This tungsten oxide/carbide SHC is active in both acidic and neutral electrolytes with a current density of 20 mA cm^{-2} at 0.32 mg cm^{-2} at overpotentials of −233 and −292 mV, respectively.[20] Likewise, Guo, *et al.* have performed the interfacial engineering of W$_2$N/WC heterostructures *via* a facile solid-state synthesis strategy.[21] Although the practical construction of W$_x$C-based heterojunction catalysts can improve the HER performance in alkaline conditions, they still have reasonably high overpotentials at high current densities (*e.g.*, 1000 mA cm^{-2}). Most synthesized catalyst layers could be easily shed from the electrode substrate due to the weak interfacial adhesion, especially at high catalytic current densities. Overall, developing highly active W$_x$C-based catalysts with long durability remains a great challenge for practical application.

[a] College of Chemistry, Fuzhou University, Fuzhou, 350116, Fujian, China

[b] CAS Key Laboratory of Design and Assembly of Functional Nanostructures, Fujian Provincial Key Laboratory of Nanomaterials, Fujian Institute of Research on the Structure of Matter, Chinese Academy of Sciences, Fuzhou 350002, China. E-mail: liuw@fjirsm.ac.cn; jianchuanyong@fjirsm.ac.cn

In this work, we prepared the large-area WS_2–WC heterojunction with abundant interfaces grown on W substrates of various shapes and sizes *via* a facile solid-state synthesis method. This proposed method is feasible for sizable self-standing W/WS_2–WC electrodes, confined only by the dimension of the growth chamber and the size of industrial-grade W substrates. The WS_2–WC heterojunction catalytic layer can form a seamless electrical contact with W substrate by strong covalent bonds, which shows superior mechanical stability to withstand the high current densities and can operate for a long-lasting lifetime for efficient hydrogen production. Consequently, the W/WS_2–WC electrode shows a low overpotential of only 58 and 473 mV at the current densities of 10 and 1000 mA cm^{-2}, respectively, along with excellent operating durability.

2.   Results and discussion

In our experiments, W substrates were used for the large-area growth of WS_2–WC flake arrays. These included the W plate, W wire, and W mesh of various sizes and shapes—as long as they could be put into the chemical vapor deposition (CVD) furnace. Fig. 1a shows that the WS_2–WC flakes were seamlessly grown on the W plate *via* a sequential two-step approach, which was plausible for industrial mass production. Firstly, a piece of W plate was directly pre-oxidized in the pressure-tight environment ($W \rightarrow WO_3$) at 800 °C in a tube furnace. Then, the WS_2–WC flakes were prepared by simultaneous sulfurization and carbonization of WO_3 in a tube furnace, using sulfur powder as a sulfur source and methane gas as a carbon source and carrier gas. The synthesis conditions were optimized to achieve high HER performance. The microscopic morphology of the W/WS_2–WC electrode was investigated *via* scanning electron microscopy (SEM). The smooth surface of the W plate (Fig. 1a and S1†) converted into compact lumps with an average size of about 0.5 μm by annealing in a pressure-tight environment, while the WO_3 lump exhibited a smooth surface (Fig. 1a and S2†). After simultaneous sulfurization and carbonization at 900 °C, the abundant flakes vertically grew on the surface of the W plate (Fig. 1a and S4†). Vertically-arranged WS_2–WC

flakes have abundant edges, which could help improve HER activity. As shown in Fig. 1b, the W/WS_2–WC electrode exhibits excellent mechanical flexibility and can be distorted many times with no visible damage, suggesting it is suitable for flexible devices in various application conditions.

X-ray diffraction (XRD) patterns indicate the successful formation of the WS_2–WC heterojunction (Fig. 2a). There are three apparent characteristic diffraction peaks of 36.1°, 37.8° and 75.2°, which can be ascribed to WS_2 (PDF# 08-0273). The other peaks of WS_2–WC heterojunction located at $2\theta \approx 32.1°$, 47.5°, 65.1°, 53.7°, 73.5°, and 77.3° can be indexed as the peaks of WC (PDF# 51-0939), which indicates that the WS_2 and WC phases are successfully synthesized. The X-ray photoelectron spectroscopy (XPS) spectra in the WS_2-WC heterojunction reveal the presence of W, C, and S elements from the full spectrum (Fig. 2b). As shown in Fig. 2c, the pronounced peaks located at the binding energies of 32.9 eV (W $4f_{7/2}$) and 35.1 eV (W $4f_{5/2}$) are assigned to the W^{4+} in WS_2–WC. The other two weak peaks located at 32.1 and 34.2 eV correspond to the features of the W–C bonds. In addition, the weaker peaks at 35.8 and 37.9 eV are ascribed to W^{6+}, respectively, suggesting that tungstic oxide exists on the sample's surface. Moreover, the S 2p core level spectrum of the WS_2–WC in Fig. 2d shows the binding energy components at 162.66 eV (S $2p_{3/2}$) and 163.85 eV (S $2p_{1/2}$) attributed to sulfide species, indicating the existence of WS_2. In Fig. 2e, the binding energy detected is referenced to the C–W species with the C 1s peak at 282.8 eV, confirming the presence of WC. The peaks at the binding energies of 284.7 eV and 286.3 eV are ascribed to the C–C and C–O species, respectively. The peak at 531.2 eV in the XPS spectra of O 1s (Fig. 2f) reveals that there are also tungstic oxides.

To analyze the multi-heterogeneous interface structure in the heterojunction, we applied high-resolution transmission electron microscopy (HRTEM) to assess the microstructure and crystal structures of the WS_2–WC heterojunction. Fig. S5† shows the typical low-magnification image of WS_2–WC on the Cu grid, which shows the flake morphologies. The HRTEM images of the WS_2–WC sample reveal the coexistence of WS_2 and WC (Fig. 3a and S6†). As shown in Fig. 3a1 and a2, the stripe spacings of 0.252 and 0.284 nm match the (100) and (001) planes of WC,
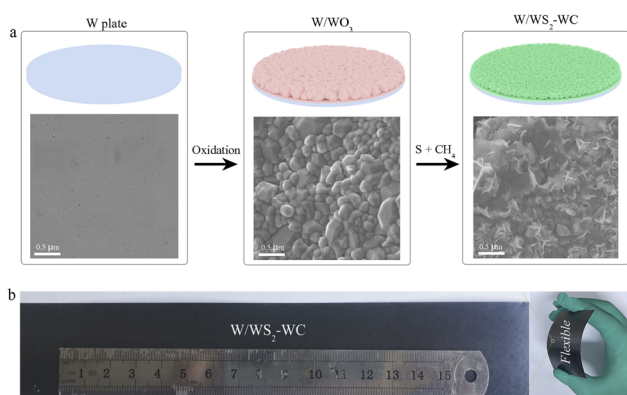

Fig. 1 (a) Schematic illustration of the fabrication process for the self-standing W/WS_2–WC electrode and corresponding SEM images. (b) Digital images of the self-standing W/WS_2–WC electrode.
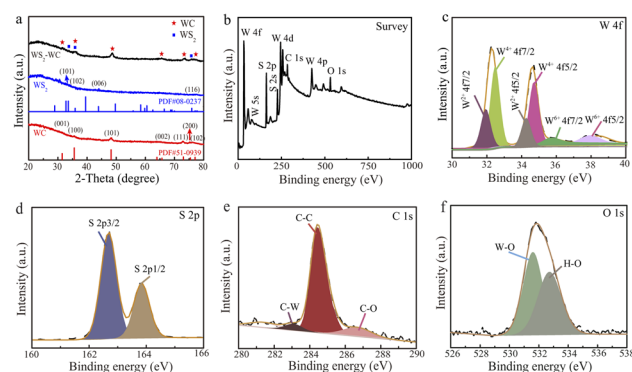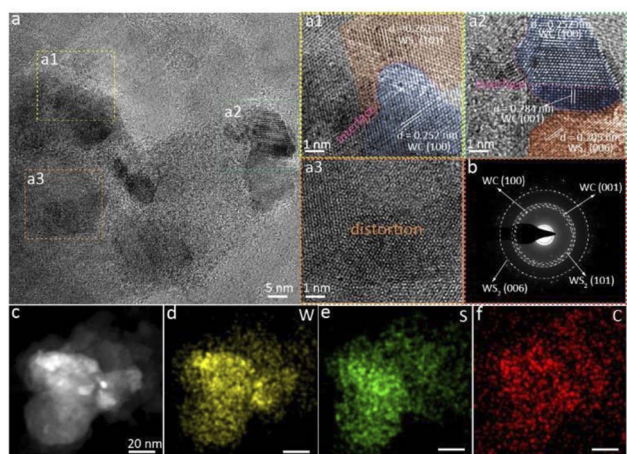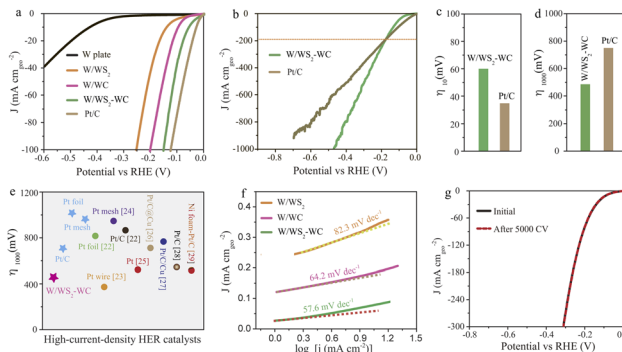

Fig. 2 (a) XRD pattern of the WS_2–WC heterojunction. (b) XPS survey of the WS_2–WC heterojunction, and high-resolution XPS of (c) W 4f, (d) S 2p1s, (e) C 1s, and (f) O 1s.

Fig. 3 (a) HRTEM images of the WS$_2$−WC heterojunction. (b) The selected area electron diffraction (SAED) patterns taken from the as-prepared WS$_2$−WC heterojunction. (c−f) Simultaneously acquired TEM images and corresponding EDS elemental mapping of (d) tungsten, (e) sulfide, and (f) carbon.

Fig. 4 (a) The HER polarization curves of different catalysts recorded in 1.0 M KOH solution. (b) Linear sweep polarization curves show the high current density behaviors of W/WS$_2$−WC and commercial Pt/C electrodes. (c and d) Corresponding overpotentials at −10 and −1000 mA cm^{-2} of the presented data in (a and b). (e) A comparison of the HER performance of the W/WS$_2$−WC electrode and Pt-based catalysts we tested and previously reported in acidic and alkaline solutions (see details in Table S1†). (f) Tafel slope of the W/WS$_2$, W/WC and W/WS$_2$−WC electrode. (g) The HER polarization curves of the W/WS$_2$-WC electrode before and after 5000 cycles in 1.0 M KOH solution.

while the apparent inter-planar spacings of 0.267 and 0.205 nm correspond to the (101) and (006) plane of WS$_2$, respectively. These abundant interfaces in the WS$_2$−WC heterojunction can induce interface charge transfer, resulting in an efficient HER activity. Meanwhile, there are also abundant defects and distortions in the structure, as shown in Fig. 3a3 and S6.† The defects can contribute to the improvement of the catalytic performance of hydrogen evolution. The corresponding selected area electron diffraction (SAED) pattern of WS$_2$−WC, shown in Fig. 3b, confirms the high crystallinity. The existence of W, C, and S elements in the material can also be verified by the EDS spectra (Fig. S7†), further supporting the formation of the WS$_2$−WC heterojunction. In addition, the EDS elemental mapping suggests that the W, S, and C elements are uniformly distributed among the entire WS$_2$−WC sample (Fig. 3c–f). These results further demonstrate the successful preparation of the WS$_2$−WC heterojunction.

The HER activities of the as-prepared electrocatalysts in the three-electrode system were conducted through a linear scan voltammogram (LSV) in H$_2$-saturated 1.0 KOH solution. Fig. 4a and b show the LSV curves at a sweep rate of 5 mV s^{-1} for different electrodes with iR correction. The potential required to reach an HER current density (j) of −10 mA cm^{-2} is an essential parameter of the HER performance. The W/WS$_2$−WC electrode exhibits small overpotentials of 58 mV at 10 mA cm^{-2} (see LSV results in Fig. 4a and c), which is better than the W plate (480 mV), W/WS$_2$ (201 mV), and W/WC (161 mV) electrode. For practical applications, the high-current-density performance of the electrocatalysts is of vital importance. The high HER performances of the W/WS$_2$−WC electrodes were optimized by controlling the co-sulfurization and carbonization temperature (Fig. S8†). Fig. 4b presents the LSV measurements performed at large current density HER. It is worth noting that the W/WS$_2$−WC electrode requires much smaller overpotentials to reach large current densities (473 mV@1000 mA cm^{-2}) than

commercial Pt/C (768 mV@1000 mA cm^{-2}), suggesting its superior performance at large current densities (Fig. 4d). Moreover, the HER performance of the W/WS$_2$−WC electrode outperformed most of the Pt-based catalysts we tested and previously reported at high current density in acidic and alkaline environments (Fig. 4e and Table S1†).[22–29]

To analyze the fundamental HER reaction kinetics mechanism occurring on the surfaces of the electrocatalysts, Tafel plots are shown in Fig. 4f (in alkaline). Interestingly, we found a small Tafel slope of 57.6 mV per decade (mV dec^{-1}) for the W/WS$_2$−WC electrode, lower than that of W/WS$_2$ (82.3 mV dec^{-1}) and W/WC electrode (64.2 mV dec^{-1}), indicating the Volmer–Heyrovsky mechanism during the HER process with the electrochemical desorption step as the rate-determining step. To further study the interfacial charge-transfer kinetics in the HER process, electrochemical impedance spectroscopy (EIS) analysis was conducted and proved that the W/WS$_2$−WC electrode generated the small charge-transfer resistances (R_{ct}) for a low onset potential and fast HER kinetics (Fig. S9†). To obtain the electrochemically active area (ECSA) of the W/WS$_2$, W/WC and W/WS$_2$−WC electrodes, the double-layer capacitance (C_{dl}) was calculated *via* cyclic voltammetry (CV). Therefore, we tested their CV curves by continuously increasing the scanning speed in the potential range of 0.1–0.2 V (Fig. S10†). The W/WS$_2$−WC electrode delivered a high C_{dl} (172.6 mF cm^{-2}), which is much higher than that of W/WS$_2$ (159.6 mF cm^{-2}) and W/WC (60.1 mF cm^{-2}). The high intrinsic HER activity for the W/WS$_2$−WC electrode is primarily derived from the flake structure, which can significantly promote electron transfer and expose more active sites. Besides the HER activity, electrochemical stability is also an important indicator of practical application. We performed long-term stability tests *via* the continuous cyclic voltammetry (CV) test for the W/WS$_2$−WC electrode, which showed significantly superior stability with no decay in alkaline

electrolytes for HER after 5000 cycles (Fig. 4g). Meanwhile, the i–t curve of the W/WS$_2$–WC electrode exhibited no significant degradation over 15 hours under alkaline conditions (Fig. S11†), further indicating its superior stability. After the stability test, the surface morphology of the W/WS$_2$–WC electrode was characterized by SEM, as shown in Fig. S12.† The comparison of the surface morphology of the WS$_2$–WC structure revealed that the detectable morphology changes could not be seen after the stability test, which indicated the excellent stability of the prepared electrode.

3. Conclusions

In conclusion, we have constructed the interfacial engineering of the WS$_2$–WC heterojunction *in situ* grown on W substrates using a facile solid synthesis strategy, which is an efficient approach to obtain abundant interfaces of long-cycling and stable electrocatalysts for HER in alkaline conditions. The unique W/WS$_2$–WC heterojunction electrode achieved a HER current density of 10 mA cm^{-2} at an overpotential of 58 mV in alkaline solution. For practical applications, the high-current-density performance of the electrocatalysts is of vital importance. It is worth noting that the W/WS$_2$–WC heterojunction electrode requires much smaller overpotentials to reach large current densities (473 mV@1000 mA cm^{-2}) than commercial Pt/C, suggesting its superior performance at large current densities. This work can provide a practical guideline to construct a heterojunction interface, thus regulating the electrocatalyst's HER performance.

Conflicts of interest

There are no conflicts to declare.

Acknowledgements

Notes and references

1 C. Y. Jian, Q. Cai, W. T. Hong and W. Liu, *J. Mater. Chem. A*, 2022, **10**, 3454–3459.

2 A. Karmakar, K. Karthick, S. Kumaravel, S. S. Sankar and S. Kundu, *Inorg. Chem.*, 2021, **60**, 2023–2036.

3 C. Y. Jian, W. T. Hong, Q. Cai and W. Liu, *J. Mater. Chem. A*, 2021, **9**, 26113–26118.

4 K. Kannimuthu, K. Sangeetha, S. Sam Sankar, A. Karmakar, R. Madhu and S. Kundu, *Inorg. Chem. Front.*, 2021, **8**, 234–272.

5 C. Y. Jian, W. T. Hong, Q. Cai, J. Li and W. Liu, *Appl. Catal., B*, 2020, **266**, 118649.

6 J. G. Li, K. F. Xie, H. C. Sun, Z. S. Li, X. Ao, Z. H. Chen, K. K. Ostrikov, C. D. Wang and W. J. Zhang, *ACS Appl. Mater. Interfaces*, 2019, **11**, 36649–36657.

7 C. Y. Jian, Q. Cai and W. Liu, *Chem. Commun.*, 2021, **57**, 11819–11822.

8 S. S. Sankar, K. Karthick, K. Sangeetha, A. Karmakar, R. Madhu and S. Kundu, *J. Mater. Chem. A*, 2021, **9**, 11961–12002.

9 S. Anantharaj, S. R. Ede, K. Karthick, S. Sam Sankar, K. Sangeetha, P. E. Karthik and S. Kundu, *Energy Environ. Sci.*, 2018, **11**, 744–771.

10 D. Zhu, L. Wang, M. Qiao and J. Liu, *Chem. Commun.*, 2020, **56**, 7159–7162.

11 W. Liu, X. T. Wang, F. wang, K. F. Du, Z. F. Zhang, Y. Z. Guo, H. Y. Yin and D. H. Wang, *Nat. Commun.*, 2021, **12**, 6776.

12 J. Zhang, T. Wang, P. Liu, Z. Q. Liao, S. H. Liu, X. D. Zhuang, M. W. Chen, E. Zscheh and X. L. Feng, *Nat. Commun.*, 2017, **8**, 15437.

13 F. Z. Song, W. Li, J. Q. Yang, G. Q. Han, P. L. Liao and Y. J. Sun, *Nat. Commun.*, 2018, **9**, 4531.

14 K. Wang, B. L. Huang, F. Lin, F. Lv, M. C. Luo, P. Zhou, Q. Liu, W. Y. Zhang, C. Yang, Y. H. Tang, Y. Yang, W. Wang, H. Wang and S. J. Guo, *Adv. Energy Mater.*, 2018, **8**, 1801891.

15 X. H. Xie, M. Song, L. G. Wang, M. H. Engelhard, L. L. Luo, A. Miller, Y. Y. Zhang, L. Du, H. L. Pan, Z. M. Nie, Y. Y. Chu, L. Estevez, Z. D. Wei, H. Liu, C. M. Wang, D. S. Li and Y. Y. Shao, *ACS Catal.*, 2019, **9**, 8712–8718.

16 J. Li, W. T. Hong, C. Y. Jian, Q. Cai, X. He and W. Liu, *J. Mater. Chem. A*, 2020, **8**, 6692–6698.

17 W. T. Hong, C. Y. Jian, G. X. Wang, X. He, J. Li, Q. Cai, Z. H. Wen and W. Liu, *Appl. Catal., B*, 2019, **251**, 213–219.

18 P. Y. Li, W. T. Hong and W. Liu, *Chin. J. Struct. Chem.*, 2021, **40**, 1365–1371.

19 A. Wu, Y. Gu, Y. Xie, C. Tian, H. Yan, D. Wang, X. Zhang, Z. Cai and H. Fu, *ACS Appl. Mater. Interfaces*, 2019, **11**, 25986–25995.

20 Y. Cui, X. Tan, K. Xiao, S. Zhao, N. M. Bedford, Y. Liu, Z. Wang, K.-H. Wu, J. Pan, W. H. Saputera, S. Cheong, R. D. Tilley, S. C. Smith, J. Yun, L. Dai, R. Amal and D.-W. Wang, *ACS Energy Lett.*, 2020, **5**, 3560.

21 J. X. Diao, Y. Qiu, S. Q. Liu, W. T. Wang, K. Chen, H. L. Li, W. Y. Yuan, Y. T. Qu and X. H. Guo, *Adv. Mater.*, 2019, **32**, 1905679.

22 Y. T. Luo, L. Tang, U. Khan, Q. M. Yu, H. M. Cheng, X. L. Zou and B. L. Liu, *Nat. Commun.*, 2019, **10**, 269.

23 L. Yu, I. K. Mishra, Y. L. Xie, H. Q. Zhou, J. Y. Sun, J. Q. Zhou, Y. Z. Ni, D. Luo, F. Yu, Y. Yu, S. Chen and Z. F. Ren, *Nano Energy*, 2018, **53**, 492–500.

24 C. Zhang, Y. T. Luo, J. Y. Tan, Q. M. Yu, F. N. Yang, Z. Y. Zhang, L. S. Yang, H. M. Cheng and B. L. Liu, *Nat. Commun.*, 2020, **11**, 3724.

25 Y. T. Luo, Z. Y. Zhang, F. N. Yang, J. Li, Z. B. Liu, W. C. Ren, S. Zhang and B. L. Liu, *Energy Environ. Sci.*, 2021, **14**, 4610–4619.

26 Y. S. Tan, R. K. Xie, S. Y. Zhao, X. K. Lu, L. X. Liu, F. J. Zhao, C. Z. Li, H. Jiang, G. L. Chai, D. J. L. Brett, P. R. Shearing, G. J. He and I. P. Parkin, *Adv. Funct. Mater.*, 2021, **31**, 2105579.

27 A. Kumar, V. Q. Bui, J. Lee, A. R. Jadhav, Y. Hwang, M. G. Kim, Y. Kawazoe and H. Lee, *ACS Energy Lett.*, 2021, **6**, 354–363.

28 R. Liu, Z. C. Gong, J. B. Liu, J. C. Dong, J. W. Liao, H. Liu, H. K. Huang, J. J. Liu, M. M. Yan, K. Huang, H. S. Gong, J. Zhu, C. Y. Cui, G. L. Ye and H. L. Fei, *Adv. Mater.*, 2021, **33**, 2103533.

29 S. Riyajuddin, K. Azmi, M. Pahuja, S. Kumar, T. Maruyama, C. Bera and K. Ghosh, *ACS Nano*, 2021, **15**, 5586–5599.